Research Article Vol. 29, No. 13 / 21 June 2021 / *Optics Express* 19903

Optics EXPRESS

Light-trapping structures for planar solar cells inspired by transformation optics

PRERAK DHAWAN,[1,*] MARIA GAUDIG,[2] ALEXANDER SPRAFKE,[2] RALF B. WEHRSPOHN,[2] AND CARSTEN ROCKSTUHL[1,3]

[1] *Institute of Theoretical Solid State Physics, Karlsruhe Institute of Technology, 76131 Karlsruhe, Germany*
[2] *Institute of Physics, Martin Luther University Halle-Wittenberg, Heinrich-Damerow-Str. 4, 06120 Halle (Saale), Germany*
[3] *Institute of Nanotechnology, Karlsruhe Institute of Technology, 76344 Eggenstein-Leopoldshafen, Germany*
[*] *prerak.dhawan@kit.edu*

Abstract: Optimal light absorption is decisive in obtaining high-efficiency solar cells. An established, if not to say the established, approach is to texture the interface of the light-absorbing layer with a suitable microstructure. However, structuring the light-absorbing layer is detrimental concerning its electrical properties due to an increased surface recombination rate (owing to enlarged surface area and surface defects) caused by the direct patterning process itself. This effect lowers the efficiency of the final solar cells. To circumvent this drawback, this work theoretically explores a transformation optics (TrO) inspired approach to map the nanopatterned texture onto a planar equivalent. This offers a pattern with the same optical functionality but with much improved electrical properties. Schwarz-Christoffel mappings are used for ensuring conformality of the maps. It leads to planar, inhomogeneous, dielectric-only materials for the light trapping structure to be placed on top of the planar light-absorbing layer. Such a design strategy paves a way towards a novel approach for implementing light-trapping structures into planar solar cells.

1. Introduction

Silicon solar cells continue to be an integral part of the growing sustainable energy market. Wafer-based crystalline silicon (c-Si) solar cells of thicknesses between $100 - 250$ μm yield strong absorption of the incident solar power. Reducing the wafer thickness below 100 μm would be interesting for solar cells as the non-radiative bulk recombination decreases and material cost can be saved. However, this approach comes at the expense of a lower light absorption [1].

Pyramidal textures with spatial footprints in the microns range are industry standard in the case of wafer-based Silicon cells [2,3]. To maximize the absorption of the incident light and thus increase the energy conversion efficiency of wafer-based and thin-film solar cells, light trapping and light management strategies have been extensively explored over the past few years by several research groups [4,5]. For thin c-Si solar cells of thicknesses <50 μm, light trapping designs have been proposed to enhance light incoupling and increase light scattering in the absorber layer using periodic or disordered nanostructures, [6–13], or enhancing resonant coupling to guided modes [14–16]. Most such approaches require direct nanostructuring of the front and/or back interfaces of the absorbing layer. The downside of nanostructuring is that it inevitably leads to an enlargement of the interface area. Thus the density of electronic defect sites per projected unit increases. Furthermore, the texturing process itself frequently introduces a significant amount of additional defect sites [17]. Therefore, surface recombination of minority charge carriers is increased, and an enhanced generation of electron-hole pairs resulting from increased absorption from texturing is significantly thwarted due to poor electrical performance [17–20]. This challenge due to increased surface recombination can be overcome by suitable passivation

#426712 https://doi.org/10.1364/OE.426712
Journal © 2021 Received 20 Apr 2021; revised 26 May 2021; accepted 27 May 2021; published 10 Jun 2021

layers on the textured surface and the use of modern solar cell concepts (heterojunctions and IBC solar cells) [21]. To provide a further solution to this problem, this work focuses on retaining the electrical performance of the un-patterned solar cell while having a superior optical response by utilizing the principles from Transformation Optics (TrO). The key idea of the suggested approach is to consider a light-absorbing layer with a nanotextured pattern that is beneficial for the light management. Then, we map this nanotextured interface to a planar interface while transforming the dielectric space above it. Figure 1 illustrates this idea, where the upper-half space of a nanostructured interface (shown on the left in grey) is mapped to a planar layer with an inhomogeneous (but smoothly varying) refractive index distribution (shown on the right with color gradient), which is directly applied on top of a planar solar cell. The structure is supposed to act optically in the same manner as the nanotextured interface, but now on top of the light-absorbing layer with planar interfaces. This renders the final device superior concerning its electrical properties. Previous research efforts of using TrO have been mainly in the field of metasurface cloaks [22–26], waveguide bends [27–29], plasmonic nanoantennas [30,31], and flattened lenses and reflectors [32–35]. For an extensive review of applicability of TrO and its future prospects, the reader is highly encouraged to refer [36,37] for an overview. In the context of solar cells, TrO has been used for cloaking the electrical contact fingers on a solar cell [38,39]. Perfect elimination of Fresnel reflection using TrO for light extraction from light-emitting-diode (LED) has also been demonstrated, which could also be used for light-incoupling into solar cells [40]. However, while being a perfect out-coupler, such a device would not capitalize on the absorption occurring over multiple passes and, thus, not being ideal for thin solar cells.

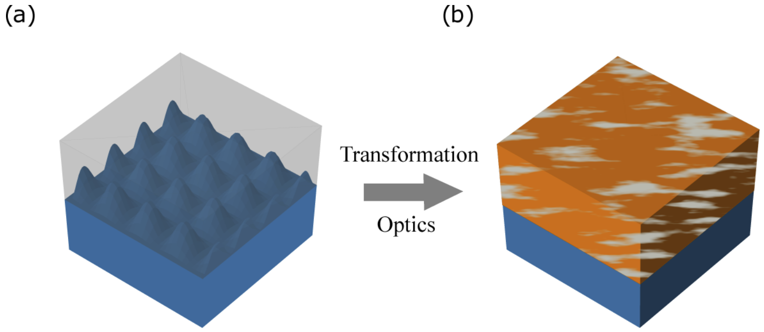

Fig. 1. Schematic diagram of the proposed idea for mapping (a) a nanostructured surface to (b) an optically equivalent planar layer with inhomogeneous refractive index.

We stress at this point that the general idea of having optically textured but electrically flat interfaces in the context of solar cells has been discussed in the past multiple times. This happened because of technological demands, for example, when considering liquid phase crystallized silicon thin-film solar cells on glass [41], or out of a general desire [42]. Then, dedicated grating-like structures were identified that serve the purpose of light management, but they were instead designed in the context of classical diffractive optical elements and not exploiting the ideas of transformation optics.

With our suggested approach in the context of light management for solar cells, we unlock a new field of applications for TrO. After a summary of the necessary background from the field of TrO, we discuss the details of the specific structures and consider their functionality in a model system of a solar cell. We initially consider modulated interfaces to demonstrate the design approach and consider selected nanotextured interfaces at a later stage. The functionality of the devices is verified in full-wave optical simulations and compared to the functionality of referential structures containing the actual nanotextured interface and other referential structures for light management to judge the improvement.

2. Background on transformation optics

The theory of transformation optics (TrO) provides a methodology for controlling the properties of light by altering material parameters spatially in a sophisticated manner. It is based on the fact that Maxwell's equations are form-invariant to coordinate transformations [43]. The deformation imposed by a coordinate transformation is interpreted as a change in the material properties of the medium as a result of the transformation. This is possible because the transformation of the space and the material parameters appear together in the Maxwell equations. This alters the propagation of light in the corresponding medium [22,23]. Considering the transformation from a Cartesian system, the electric permittivity ϵ' and magnetic permeability μ' of the transformed medium are obtained from:

$$\begin{aligned} \underline{\underline{\epsilon'}} &= \frac{J\epsilon_r J^T}{\det(J)}, \\ \underline{\underline{\mu'}} &= \frac{J\mu_r J^T}{\det(J)}, \end{aligned} \tag{1}$$

where ϵ_r and μ_r are the permittivity and permeability of the embedding isotropic medium in the Cartesian coordinates, respectively, and J is the Jacobian for the transformation. If we restrict ourselves to two dimensions, one can find a mapping $w : \mathbb{C} \to \mathbb{C}$ where the real and imaginary parts of the transformation represent the coordinates in the new space. If the transformation from $w = x' + iy'$ to $z = x + iy$ satisfies the Cauchy Riemann conditions:

$$\frac{\partial x'}{\partial x} = \frac{\partial y'}{\partial y} \quad \frac{\partial y'}{\partial x} = -\frac{\partial x'}{\partial y}, \tag{2}$$

and w is differentiable in a region Λ, then the mapping is conformal in nature. For such mapping, the structure will be uniaxial anisotropic and inhomogeneous with permittivity and permeability tensors reducing to a simple form:

$$\begin{aligned} \underline{\underline{\epsilon'}} &= \operatorname{diag}\left(1, 1, \frac{1}{\det(J)}\right)\epsilon_r, \\ \underline{\underline{\mu'}} &= \operatorname{diag}\left(1, 1, \frac{1}{\det(J)}\right)\mu_r. \end{aligned} \tag{3}$$

For TE polarization with the material in the Cartesian space assumed to be non-magnetic ($\epsilon_z, \mu_x = 1, \mu_y = 1$), therefore, the only parameter to be controlled in the transformed space is the refractive index ($\mu = 1$ and $n = \sqrt{\epsilon_z}$), which for a mapping defined from corrugated texture to a planar geometry yields:

$$n'(x', y') = n_0 \left|\frac{dw}{dz}\right|, \tag{4}$$

with n_0, the refractive index of the untransformed dielectric half-space [32]. For our purpose, n_0 is chosen to be the refractive index of Ethyl-vinyl Acetate (EVA), which is the common encapsulant for the solar cell when building a solar module. For simplicity, EVA is taken to be non-dispersive in the wavelength range of interest with value $n_0 = 1.5$. This way, we restrict to only dielectric materials for the designed structure.

3. Cell design and simulation

To understand the light-trapping behavior of the nanostructured and the transformed systems, we consider a simple solar cell consisting of a 1 μm thick c-Si layer equipped with an Ag back-reflector, see Fig. 2(a) for the actual reference structure and Fig. 2(b) for its planarized counterpart. We choose 1 μm thick Si cells for our study to allow for a more broadband investigation of absorption enhancement thanks to the light trapping effect of the textured interface. For much thicker solar cells, this tends to have a less noticeable impact. The metal back-reflector is used to reflect light that the c-Si has not absorbed in a single pass. The dispersive permittivities of these materials are taken from literature [44,45]. The space above the light absorber is semi-infinite and filled with EVA. With that, the structure corresponds to a prototypical geometry representative of an encapsulated solar cell. Simulations are carried out using an in-house Finite-Difference Frequency-Domain (FDFD) code for TE polarization at normal incidence with a spatial resolution of 4 nm. Periodic boundary conditions (PBC) and perfectly matched layers (PML) are applied along the transverse and longitudinal direction, respectively. Using TrO, the inhomogeneous refractive index is determined for the design region Ω placed above the planar c-Si layer. For different textures in consideration, the volume of the absorbing layer is always kept constant to eliminate any trivial absorption gain.

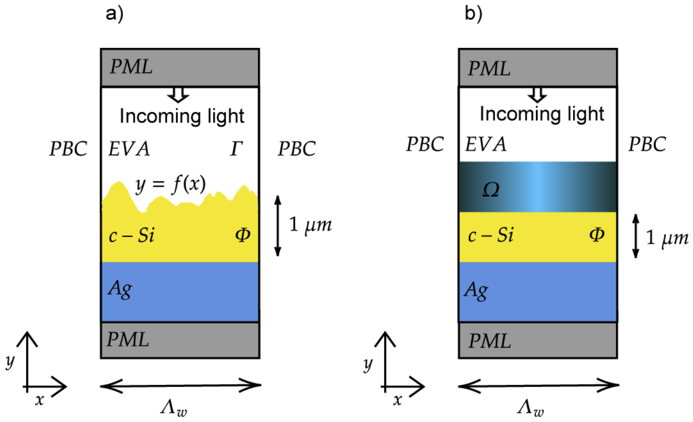

Fig. 2. (a) Textured absorbing layer with perfecly matched layers (PML) and periodic boundary conditions (PBC). (b) Desired geometry with inhomogeneous, non-absorbing design domain Ω obtained by mapping Γ to Ω.

4. Schwarz Christoffel mapping for light-trapping structures

Section 2 showed that we must restrict ourselves to conformal maps for obtaining isotropic medium as the final structure in the physical space. Schwarz Christoffel (SC) transformations are one set of such conformal maps that provide a straightforward way to conformally map the interior of a polygon with m vertices onto the complex upper-half-space. The SC transformation is given by:

$$w = f(z) = f(z_0) + C \int_{z_0}^{z} \prod_{i=1}^{m} (\tilde{z} - z_i)^{(\phi_i/\pi)-1} d\tilde{z}, \tag{5}$$

where ϕ_i is the angle subtended by the i$^{\text{th}}$ corner, and $f(z_0)$ and C are complex constants for translating and scaling the map, respectively. We will use in the following a SC transformation to map the half-space above the light-absorbing layer of our solar cell that contains the nanotexture to a planar interface. Since such a mapping is conformal, the texture used for our study is one-dimensional. These mappings are numerically generated using MATLAB SC Toolbox [46].

For implementing the SC transformation, the open polygon for the w-space is defined by the points defining the texture profile with one of the vertices at infinity. This is used as the lower boundary of the coordinate transformation. This open polygon is then mapped to the complex upper-half plane such that $f(\infty) = \infty$. The resulting SC transformation then ensures that the optical path length between two points z_1 and z_2 in the physical space is equal to the optical path length between points $f(z_1)$ and $f(z_2)$ in the virtual space above the textured interface [35].

To account for the periodicity of the texture, the prevertices of a periodic unit cell Λ_w in the virtual space are scaled using the complex constant C from Eq. (5) so that they effectively map to the same length of a periodic unit cell in the physical space, Λ_z (region obtained as a result of mapping the virtual space). This scaling maintains the periodicity of the structure so that identical diffractive features appear. Since the software package used does not support periodic boundary conditions, we transform a larger super-periodic structure of multiple unit cells. Afterward, the scaling of the SC map is done over this larger structure to still achieve similar periodicity. We then resort to using only the central spatial domain of this structure with periodic boundary conditions for simulations. To estimate the accuracy of this scaling, a normalized error function depending on the number of periodic unit cells N is considered for the analysis, which is defined by:

$$\delta(N) = \frac{|\Lambda_z - \Lambda_w|}{\Lambda_w} \; \forall \, z \in \Omega \,|\, f(z) \in \Gamma, \tag{6}$$

where Ω is the design region in physical space and Γ is the region in the virtual space. For our analysis, values that satisfy the equation $\log_{10}(\delta) \leq -2$ obtained for $n \geq 15$ for periodic structures and $N \geq 7$ for disordered structures were found to be sufficient to avoid edge-effects from the maps while still retaining the accuracy of the obtained maps [47].

We stress upfront that our approach does not aim to map the entire space but only the space above the textured interface. This is because for the geometry in consideration, given a map for one of the half-spaces, it is impossible to find an analytical continuation into the other half-space. Moreover, an individual mapping of the upper and lower half-space would lead to a spatially inhomogeneous and dispersive light-absorbing layer, which is neither feasible nor desirable. Our obtained transformations, therefore, strictly speaking, are incomplete, and the transformed structure will not exactly optically respond as the original one. Nevertheless, the preservation of optical path length in the virtual space and its corresponding points in physical space yields a spatially inhomogeneous material distribution in physical space with regions of a high and low refractive index such that it offers similar diffractive features as the related textured interface. The structures perceived with this approach then continue to serve their purpose for our discussion. We, therefore, rather speak of a transformation optics-inspired approach in the context of light-trapping.

4.1. Periodic texture

To illustrate the practical aspects of our approach, we first study a sinusoidal interface between a c-Si and a dielectric half-space (EVA). At a later stage, arbitrary profiles are considered that resemble textured interfaces. However, the methodology to study such complex textures will be analog to that for a sinusoidal interface.

Figure 3(a) shows the mapping obtained in the w-plane (virtual space) when the upper half of the complex plane is mapped to the open polygon defined by the space above the sinusoidal texture with a lattice period $\Lambda_w = 0.3$ μm and height $H = 2A = 0.2$ μm where A is the amplitude of the modulation. Using Eq. (4), we then arrive at the desired refractive index distribution in the physical space for our planar system. Figure 3(b) shows this refractive index distribution with n_0 taken to be the refractive index of the EVA layer. The curved grid lines in this sub-figure show the mapping in the physical space due to an inverse transformation that maps an overlaid Cartesian grid above the textured interface (region containing homogeneous material) to the complex upper-half space in this sub-figure physical space.

The SC mapping applies to the entire upper-half-space. Nevertheless, for computational purpose, a finite domain has to be considered characterized by a sufficient longitudinal length T in where the refractive index distribution is transformed. The spatial extent is chosen such that the index at the terminating interface to the surrounding matches very well with the refractive index of the untransformed homogeneous EVA layer. This longitudinal length is limited to $T = 0.25$ μm

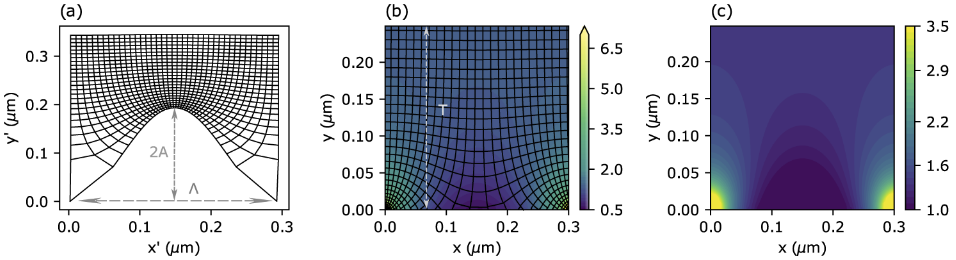

Fig. 3. (a) Spatial grid for the virtual space (w-space) obtained by mapping the complex upper-half-space to the open polygon with a sinusoidal texture with lattice period $\Lambda_w = 0.3\ \mu$m and height $H = 2A = 0.2\ \mu$m. (b) Refractive index and its overlaid spatial grid in the physical space (z-space) obtained using inverse transformation. The domain is longitudinally extended till $T = 0.25\ \mu$m. (c) Refractive index in the physical space after truncating its limit to [1-3.5]

for our designed sinusoidal texture, and it is changed in accordance with the properties of the texture in consideration. While the derived refractive index in the physical space ranges from $n(\Omega) = [0.5, 81]$, for reasons of feasibility, this range is truncated to the limits $n(\Omega) = [1, 3.5]$ where the lower limit is permitted to be less than the refractive index of the EVA. This limit is put forward by available materials and the finite parameter range they offer. This range for the inhomogeneous distribution is maintained throughout this paper. Figure 3(c) shows the refractive index in the physical space after truncating it to this range.

The curved grid lines in the z-plane from inverse transformation and its resulting refractive index distribution, as shown in Figs. 3(b) and (c), can intuitively be understood as:

- Dilation in space as a result of 'flattening' of the bumps. This leads to regions having sub-unity refractive indices in the central region ($x = 0.15\ \mu$m).
- Consequent compression of space in the surrounding region of the dilated space to maintain conformality of the map. This leads to regions having very high refractive index at the edges ($x = 0$ and $x = 0.3\ \mu$m).

4.2. Disordered texture

Following the same approach as the sinusoidal texture, a disordered texture is considered here for a strongly scattering response and a more broadband absorption enhancement. This randomized texture is described by its root mean square (RMS) roughness σ, and a lateral correlation length ζ is considered. The latter property is defined as the distance at which the correlation function $W(s) = e^{-s^2/\zeta^2}$ decreases by $1/e$ [48].

Figure 4 shows a textured interface with correlation length $\zeta = 0.15\ \mu$m and RMS height $\sigma = 0.2\ \mu$m and its derived refractive index distribution in the physical space truncated to bounds $n(\Omega) = [1, 3.5]$. For the texture profile to be differentiable everywhere and to avoid extremely large derivatives in the conformal map, a Gaussian function with statistical parameters σ and ζ is investigated for the surface texture described as [49]:

$$y(x) = \sigma\sqrt{\frac{2}{L}}\sum_{m=1}^{\infty}\tilde{P}\left(mk_0\right)\left[\alpha_{2m-1}\sin(mk_0x) + \alpha_{2m}\cos(mk_0x)\right], \tag{7}$$

where α is a normally distributed random number [50]. We consider a sufficient large super periodic structure for the textured interface that is characterized by a spatial extent of Λ. The modulations, therefore, appear at spatial frequencies integer multiples of $k_0 = 2\pi/\Lambda$.

$\tilde{P}(k) = \sqrt{\pi}\zeta e^{-\zeta^2 k^2/4}$ is the power spectrum in the reciprocal space. The spatial extent of one lattice period of the textured interface is taken to be between 12 μm and 15 μm. Choosing this large lattice period when compared to the typical correlation lengths in consideration suppresses possible artifacts from the periodicity and provides statistically stable results. Also, using sufficiently large simulation domains allows us to take smaller numbers of periodic elements for the SC maps, thus relieving the computational overhead arriving from transforming a super-periodic structure. For maintaining proper periodicity, the disordered texture is truncated in the simulation domain by multiplying the randomized function with a tapered cosine window given by [51]:

$$w(x) = \begin{cases} \frac{1}{2}\left\{1+\cos\left(\frac{2\pi}{r}(x-r/2)\right)\right\}, & 0 \le x < \frac{r}{2} \\ 1, & \frac{r}{2} \le x < 1-\frac{r}{2} \\ \frac{1}{2}\left\{1+\cos\left(\frac{2\pi}{r}(x-1+r/2)\right)\right\}, & 1-\frac{r}{2} \le x \le 1 \end{cases} \tag{8}$$

where x ranges from 0 to 1 and r is the shape factor of the window, giving the fraction of the window inside the tapered-cosine segment. For this work, a moderate value of $r = 0.2$ was used for the simulations to retain properties of the characteristic disorder and avoid spurious resonant modes arriving due to sharp tapering. The impact of using this window function for the simulations is beyond the scope of this paper, and the reader is encouraged to refer to [52] for an overview.

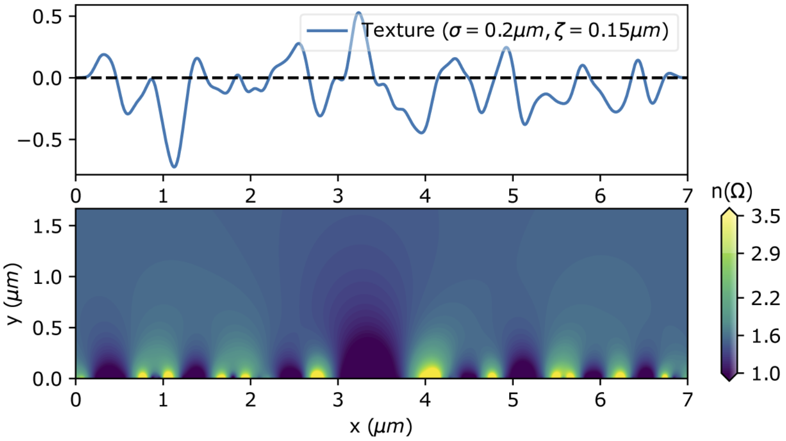

Fig. 4. Textured interface with correlation length $\zeta = 0.15$ μm and RMS height $\sigma = 0.2$ μm and its resulting refractive index distribution in physical space after transformation.

5. Optical response of the structures

5.1. Periodic

We consider at first a sinusoidally textured interface with a lattice period of $\Lambda = 0.3$ μm and height $H = 2A = 0.2$ μm where A is the modulation amplitude. For the given modulation amplitude, this lattice period was found to be optimal to maximize the photocurrent J_{ph}. Figure 5(a) shows the numerically simulated absorption in the c-Si layer for the textured interface, its counterpart perceived using TrO, and a reference structure with a planar interface but a linear graded-index anti-reflective (AR) coating with a thickness of $T = 1$ μm. The thickness of this AR coating is kept large for broadband antireflection. As a useful comparison to the TrO structure, the refractive index of this coating is kept in the range $[1.5, 3.5]$ so that it is impedance-matched with the EVA layer.

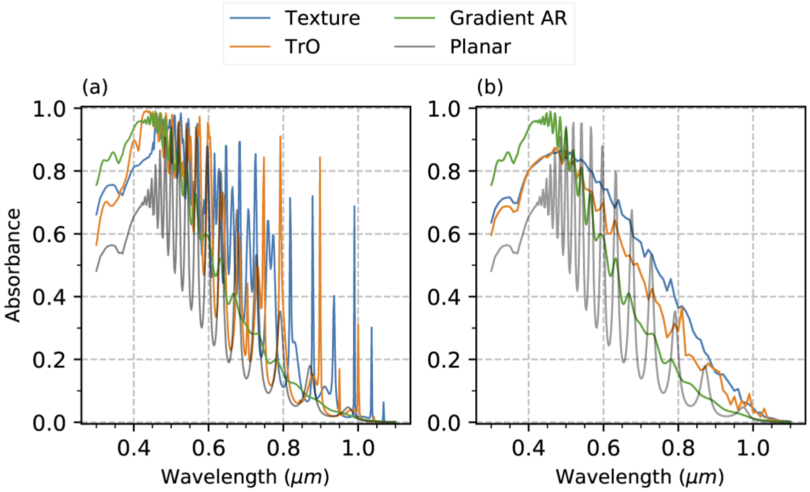

Fig. 5. Absorption spectrum obtained using a periodic and disordered texture (blue) and its planar counterpart (orange) derived using SC mapping are plotted. As references spectra, the absorption of a planar c-Si wafer (grey) and of a planar interface with additional linear graded index AR layer (green) are illustrated. (a) Sinusoidal texture with height $H = 2A = 0.2$ μm and lattice period $\Lambda = 0.3$ μm. (b) Disordered texture with RMS roughness $\sigma = 0.2$ μm and correlation length $\zeta = 0.15$ μm.

For the flat structure without any texture or the inhomogeneous index layers (TrO or gradient AR coating), the absorbing layer acts as a Fabry-Perot cavity with its absorbance obeying the corresponding resonance peaks. Upon introducing the texturing or the inhomogeneous layers, the short and long-wavelength ranges show higher absorption than the planar structure. For shorter wavelengths where c-Si is highly absorbing, light is absorbed before reaching the metal back contact. The enhanced in-coupling of the light is sufficient for giving high absorption enhancements. For this regime, the gradient AR coating provides a stronger in-coupling of light than the sinusoidal texture. For wavelengths longer than 500 nm where 1 μm thick c-Si is weakly absorbing, the objective is now to excite the higher diffraction orders solely as they correspond to longer path lengths of light in the absorbing media. In this regime, the AR coating fails in scattering light into these diffraction orders compared to the texture [53]. The TrO structure, as shown in Fig. 3(b), is observed to be a decent trade-off between these two in terms of encompassing both anti-reflective and light scattering properties. The structure is found to have an anti-reflective effect for the $0.3 - 0.4$ μm wavelength range as a result of smooth variation in refractive index along both lateral and longitudinal direction. The scattering properties of this structure are better evaluated for the weakly absorbing wavelength range between $0.45 - 0.6$ μm where due to the refractive index variation in the lateral direction, excitation of higher diffraction orders of the structure is observed. For the longer wavelength range between $0.6 - 1.1\mu$m, the lateral features in the TrO structure are not perceived by the incident light, and it merely acts as an effectively averaged medium, thus decreasing the impedance mismatch between the EVA and the Silicon layer.

5.2. Disordered structure

Figure 5(b) shows the absorption spectrum obtained for a planar c-Si using the inhomogeneous layer derived from SC map in comparison to the spectrum of the respective disordered texture with an RMS roughness of 0.2 μm and a correlation length of 0.15 μm. This correlation length was optimal for a fixed RMS roughness to maximize the photocurrent. The absorption spectra shown in Fig. 5(b) for both the geometries are averaged over the absorption spectra obtained from 3 surface realizations with nominally identical properties.

Similar to the discussion for the periodic structures, the gradient AR coating again outperforms the disordered texture at shorter wavelengths due to its strong light in-coupling. For wavelengths longer than 500 nm, we observe the benefits of the disorder as it offers more scattering channels, thus giving more broadband absorption enhancement when compared to the periodic structure. The TrO structure obtained from the disordered texture continues to serve as a trade-off between the gradient AR coating and the texture only this time, surpassing its periodic counterpart. However, the absorption spectrum for the TrO structure [shown by the orange curve in Fig. 5(b)] shows less smearing of Fabry-Perot oscillation peaks than its disordered counterpart, thus implying that it cannot capitalize over the populated Fourier spectrum offered by the disorder. This can be ascribed to finer details of the disorder partially getting washed away due to refractive index capping (as indicated in Section 1).

6. Photocurrent of the obtained devices

We calculate the photocurrent J_{ph} for each solar cell geometry using:

$$J_{\text{ph}} = e\int_{\lambda_1}^{\lambda_2} \varphi(\lambda)A_{\text{total}}(\lambda)\eta_{\text{IQE}}d\lambda, \tag{9}$$

where $\varphi(\lambda)$ is the AM1.5G solar irradiation spectrum. For simplicity, the internal quantum efficiency η_{IQE} is taken to be 1. Using the spatially dependent electric field distribution from the simulation, the global absorption in Silicon is calculated by integrating the local absorption across the spatial extent of the absorbing layer. This is given by:

$$A_{\text{total}}(\lambda) = \frac{\omega}{2}\epsilon_0\Im(\epsilon(\lambda))\int_{\Phi}\left|E_z(\vec{r},\lambda)\right|^2 dV, \tag{10}$$

where $\omega = \frac{2\pi c}{\lambda}$ is the frequency of incident light. For determining J_{ph}, this absorption is calculated from $\lambda_1 = 300$ nm to $\lambda_2 = 1100$ nm in steps of 2 nm for periodic structures and 10 nm for disordered structures.

6.1. Periodic

Using Eq. (9), the photocurrent is calculated for these structures in the short (300-500 nm) and long (500-1100 nm) wavelength range and summarized in Table 1. We also add the total photocurrent resulting thereof for convenience to the table.

As discussed in Sec. 5, the AR action noted for both the texture as well as the TrO structure is evident in their similar J_{ph} for 300-500 nm wavelength range. The gradient AR coating outperforms both these structures in the 300-500 nm regime with a larger J_{ph}, but this gain is compromised at the longer wavelength range 500-1100 nm, where scattering into multiple channels becomes important.

Table 1. Comparison of photocurrent for sinusoidal texture of height $H = 2A = 0.2\ \mu$m and lattice period $\Lambda = 0.3\ \mu$m, TrO geometry and planar references.

J_{ph} (mA/cm^2)	Texture	TrO	Gradient AR	Planar
300-500 nm	5.48	5.67	5.87	4.29
500-1100 nm	14.10	12.13	10.31	9.14
300-1100 nm	19.58	17.80	16.18	13.43

6.2. Disordered

Table 2 summarizes the J_{ph} for the texture with fixed RMS height $\sigma = 0.2$ μm and Correlation length $\zeta = 0.15$ μm in comparison to the other references. Similar to the discussion in Sec. 6.1, the TrO structure serves to be a decent trade-off between the textured interface and the gradient AR layer as it yields comparable J_{ph} for the short wavelength range and large J_{ph} in comparison to the gradient AR layer for the longer wavelength range. A similar correlation between the disordered texture in consideration and its planar counterpart is analyzed here where we show averaged J_{ph} for both the geometries as a function of σ and ζ in Figs. 6(a) and (b). At the same time, the other parameter is kept fixed, respectively.

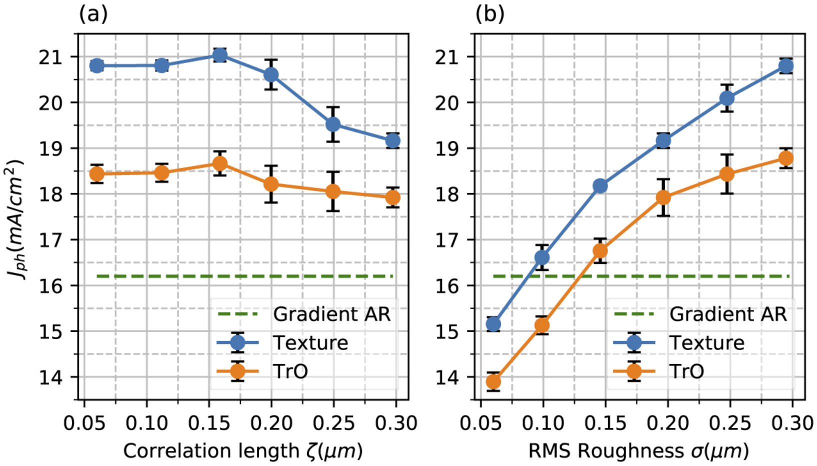

Fig. 6. Comparison study of J_{ph} as a function of correlation length and RMS height for a disordered structure. (a) RMS roughness $\sigma = 0.2$ μm. (b) Correlation length $\zeta = 0.3$ μm. The errorbars indicate the standard deviation of J_{ph} from the conducted trials.

Table 2. Comparison of photocurrent for a disordered texture of RMS height $\sigma = 0.2$ μm and Correlation length $\zeta = 0.15$ μm, TrO geometry and planar references.

J_{ph} (mA/cm^2)	Texture	TrO	Gradient AR	Planar
300-500 nm	5.02	4.97	5.87	4.29
500-1100 nm	16.02	13.69	10.31	9.14
300-1100 nm	21.04	18.66	16.18	13.43

Figures 6(a) and (b) suggest that the TrO model can acquire the stochastic nature of the disordered texture in the index distribution. While the TrO geometry follows a similar trend for J_{ph} as the texture, the discrepancy between the two geometries increases on average for sharper features. This is not surprising as it means obtaining more extreme refractive indices in the physical domain from the SC map. For shorter correlation lengths (ζ<0.15 μm) with fixed RMS roughness ($\sigma = 0.2$ μm), the features of the texture are very sharp and the light can neither spatially resolve the texture nor the spatial features in the inhomogeneous TrO layer. Consequently, the contribution to high J_{ph} indicated in Fig. 6(a) for these structures mainly comes from the anti-reflective effects it provides [6]. Also, due to the sharp features in small lateral lengths, the SC maps now, on average, encompasses stronger derivatives in the physical space. This vital information of the texture properties ends up being ignored in the simulation due to refractive index capping, thereby explaining the larger discrepancy in the TrO geometry despite the texture not being optimal.

The discrepancy in J_{ph} between the texture and the TrO structure is further studied in Fig. 6(b) by fixing the correlation length with the minimum difference in J_{ph} ($\zeta = 0.3\ \mu$m) and varying the RMS roughness of the texture. For larger RMS roughness ($\sigma > 0.15\ \mu$m), a saturation of the J_{ph} curves is observed due to optimal coupling to the diffraction pathways offered by the texture and the TrO structure in consideration. Also, the increase in RMS roughness requires more compression in the physical space. To preserve the optical path length in the physical space, this stronger compression comes at the expense of more extreme refractive index distribution, which, as a result of capping, then roughly translates to a larger discrepancy between the texture and the TrO structure.

Figure 7 summarizes the normalized photocurrent for nanostructures considered in comparison to the Lambertian limit for a 1-D textured interface for 1 μm thick c-Si layer. This limit is calculated using $A(\lambda) = \alpha(\lambda)L/(\alpha(\lambda)L + 1/Z(\lambda))$ where $Z(\lambda) = n(\lambda)\pi$ is the 2D bulk limit for the enhancement factor and L is the wafer thickness 1 μm [7,53,54]. The normalization factor is chosen to be J_{ph} obtained by an un-patterned 1 μm thick c-Si with a Ag back reflector.

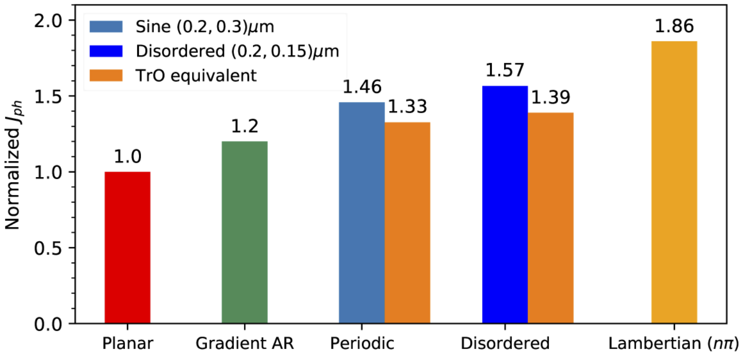

Fig. 7. Comparison of photocurrent densities J_{ph} with a flat interface. The normalized J_{ph} is calculated with respect to the 1 μm thick c-Si flat interface with Ag back-reflector: $J_{\text{ph}} = 13.43$ mA/cm^2.

Best results are reported for the structure with the disorder as it outperforms the sinusoidal periodic texture with similar height profiles, and this trend is inherited in its TrO counterpart. Also, the absorption in the c-Si layer for both the cases approaches the theoretical limit put forward by a Lambertian scatterer in two dimensions. To understand the benefits of our proposed structures, we qualitatively estimate the detrimental impact of nanostructuring by realizing that the effective front surface recombination velocity is directly related to the surface enlargement factor γ. This is the factor by which the surface area of the absorbing layer increases from nanostructuring [17]. Since our simulations are two-dimensional, we rather speak of the factor by which the length of the interface increases from texturing. For a texture whose profile is given by $y = f(x)$, the length enlargement factor E is calculated by $E = \int_0^{\Lambda} \sqrt{1 + (dy/dx)^2}dx/\Lambda$ where Λ is the periodicity of the unpatterned cell. We find that for the disordered structure with $\sigma = 0.2\ \mu$m and $\zeta = 0.15\ \mu$m, $E \approx 1.9$. This implies for the given textured interface, just the length enlargement due to texturing will almost double the surface recombination velocity when compared to the planar cell. The alternate TrO approach then becomes beneficial as the recovered electric performance from using the planar active layer can outweigh its sub-par optical performance compared to its textured counterpart.

7. Lower limit for refractive index upper-bound of TrO structures

In this section, we elaborate on the impact of choosing the upper limit for the refractive index of the TrO structure. While the consideration of choosing the previously considered upper bound for this region was to have the TrO structure better impedance-matched with the bottom c-Si layer, it is worthwhile to investigate the effect of having a lower refractive index upper bound for this layer for experimental feasibility. Figure 8 shows the effect of limiting the permissible refractive index range in the TrO model for both periodic and disordered interface compared to the refractive index range of 1 and 3.5. For a fair comparison, we also include a gradient AR layer with a refractive index range from 1.5 and 2.5.

As is to be expected, a lower upper limit for the refractive index affects the impedance matching condition for wavelengths shorter than 500 nm, thus corresponding to a decreased absorption as shown in Fig. 8. However, the effect of choosing a smaller refractive index range is less prominent for longer wavelengths where the value of the effective index which the light experiences does not change much. Table 3 summarizes the photocurrent obtained for shorter and longer wavelength range for these structures. These results are compared with a Gradient AR layer of range [1.5,2.5]. For the periodic structure, using a smaller refractive index range does not degrade its overall optical response and thus its photocurrent, but for the disordered structure, this degradation is noticeable for shorter wavelengths. However, both the cases outperform the gradient AR layer for wavelengths longer than 500 nm where as discussed earlier, the diffractive effects become important. These results indicate that while the absolute improvement might be compromised from using a smaller refractive index range, the relative improvement to the gradient AR strategy of similar refractive index upper bound still holds strong.

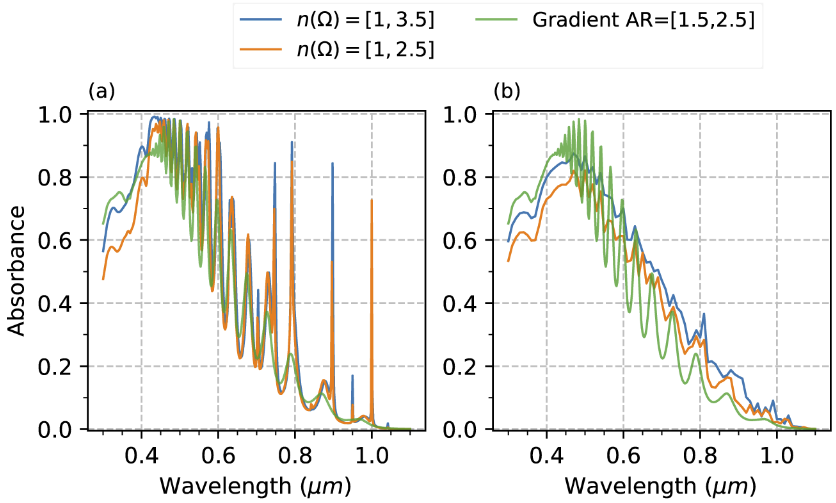

Fig. 8. Absorption spectrum obtained for TrO structures with different permissible refractive index ranges for (a) Periodic structure mapped from a sinusoidal texture with height $H = 2A = 0.2$ μm and lattice period $\Lambda = 0.3$ μm (b) Disordered structure mapped from a disordered interface of RMS roughness $\sigma = 0.2$ μm and Correlation length 0.15 μm.

Table 3. Comparison of photocurrent for periodic and disordered TrO structures for refractive index bound $n(\Omega) = [1, 2.5]$ and $n(\Omega) = [1, 3.5]$. Results are compared with Gradient AR layers of range [1.5,2.5] and [1.5,3.5].

J_{ph} (mA/cm^2)	Periodic $n(\Omega)$		Disordered $n(\Omega)$		Gradient AR	
	[1,2.5]	[1,3.5]	[1,2.5]	[1,3.5]	[1.5,2.5]	[1.5,3.5]
300-500 nm	5.35	5.67	4.55	5.21	5.38	5.87
500-1100 nm	11.30	12.13	11.94	13.69	10.05	10.31
300-1100 nm	16.65	17.80	16.49	18.66	15.43	16.18

8. Incoherent treatment of Air-EVA interface

In this section, we investigate the effect of considering the Air-EVA interface in our simulations. Since the EVA encapsulant layer is typically around 400 μm thick, it is not feasible to consider light propagation through this layer coherently but an incoherent treatment needs to be put in place. For this, we consider the simulation setup as before but now correcting for the reflection from Air-EVA layer *a posteriori* [55]. Here, in essence, we have to take into account each individual scattering path, that are defined by the spatial frequencies of our interfaces, called in the following diffraction orders. We consider the response while considering an increasing number of back-reflections of the light at the Air-EVA interface, called in the following round-trip orders. Practically, we trace in our procedure the amplitude contained in each of the diffraction orders in a sequence of increasing round trips within the EVA. This is done for each temporal frequency individually. We start by considering normal incident onto the structure where the upper half-space is filled with EVA. The amplitude of the field is corrected by an initial reflection at the Air-EVA interface (zeroth interaction of light with Air-EVA interface). A fraction of this light gets absorbed by the active region and a fraction of light is also reflected into discrete diffraction orders. Each of these diffraction orders get back-reflected onto the solar cell from the Air-EVA interface (first interaction of light with the Air-EVA interface), thereby serving as an incident field onto the active layer. Again, absorption in the active layer and distribution of back-reflected light is computed and the iteration loop is closed.

Mathematically spoken, the contribution of the j$^{\text{th}}$ round-trip order to the absorbance in the active layer is calculated as,

$$A^j = \vec{I}^j_{\text{down}} \cdot \vec{A}, \tag{11}$$

where j$^{\text{th}}$ order corresponds to the j$^{\text{th}}$ interaction of the light with the Air-EVA interface. $\vec{I}^j_{\text{down}}$ is the intensity distribution incident on the structure and is given by:

$$\vec{I}^j_{\text{down}} = \vec{I}^j_{\text{up}} \odot \vec{R}_a, \tag{12}$$

where $\odot$ denotes the element-wise multiplication of the reflectivity R_{a} for the EVA-air interface for each diffraction order and intensity distribution $\vec{I}^j_{\text{up}}$ in the j$^{\text{th}}$ round-trip order correction of the reflected light from the structure. This quantity is calculated using a scattering matrix which relates the light incident on the structure to the light reflected from it. This is given by:

$$\vec{I}^j_{\text{up}} = \underline{\underline{S}}\vec{I}^j_{\text{down}}, \tag{13}$$

where the elements of this matrix are given by:

$$S_{\text{ba}} = |E^{\text{EVA}}_{\text{ba}}|^2 \frac{\cos\theta_b}{\cos\theta_a}. \tag{14}$$

Each coefficient of this matrix relates the b^{th} diffraction order in the reflected spectra to the a^{th} diffraction order in the incident field. The absorbance in the active layer till the n^{th} round-trip order correction is then:

$$A^{\mathrm{n}}(\lambda) = \sum_{j=1}^{n} A^{\mathrm{j}}. \tag{15}$$

This process was iteratively carried out until the $A^{\mathrm{n}}(\lambda)$ converges to a value A_0 such that

$$A_0/A^{n-1} < 10^{-4}. \tag{16}$$

Figure 9 shows the absorbance in the active c-Si layer in comparison to the results without the Air-EVA interface. Periodic and Disordered textures and their corresponding TrO structures with refractive index bound of [1-3.5] were considered for this study. Figures 9(a) and (b) suggest that the absorbance calculated without considering the Air-EVA interface underestimates the absorbance in the active layer and that this correction is important for studying the behaviour of the TrO structures in a realistic environment. For shorter wavelengths, higher-order back-reflection occurs and therefore the correction factor ends up increasing the absorption in the active layer by a small amount. For the periodic structures (lattice period $\Lambda_w = 0.3$ μm), only the zeroth diffraction order exists for wavelengths longer than 450 nm and thus the first-order reflection correction is sufficient for the analysis. For the disordered structures, which have large periodicity, a considerable fraction of scattered light experiences higher-order diffraction. This fraction illuminates the interface again after reflection from the Air-EVA interface, but will mainly remain un-absorbed for wavelengths longer than 600 nm due to the very thin active layer of our study leaving the first-order correction inaccurate. We then find such a scattering matrix approach essential for the disordered structures.

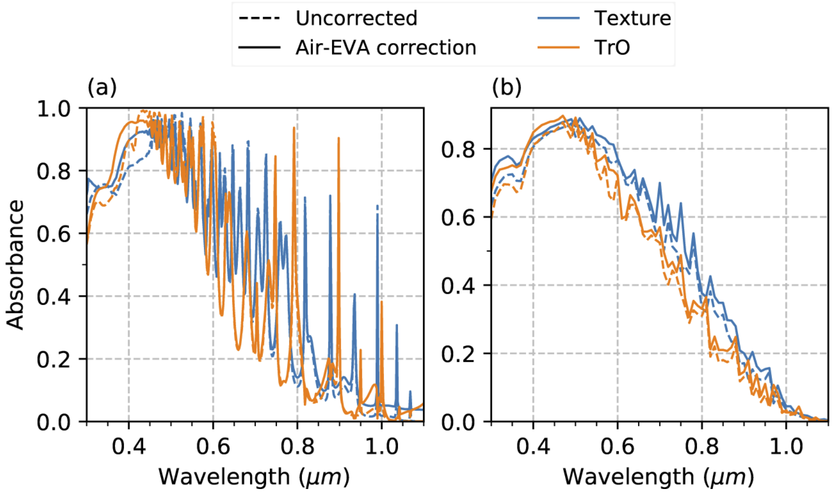

Fig. 9. Absorption spectrum obtained after considering reflection from Air-EVA interface for (a) Sinusoidal texture of height $H = 2A = 0.2$ μm and lattice period $\Lambda = 0.3$ μm and (b) for the disordered texture of RMS height $\sigma = 0.2$ μm and Correlation Length 0.15 μm.

Table 4 summarizes the photocurrent after the Air-EVA consideration. For the periodic texture and its TrO counterpart, the increase in the overall photocurrent notably comes for the wavelengths shorter than 450 nm, whereas for the disordered structure and its TrO counterpart, this increase in photocurrent is considerable for longer wavelength range as well. Through the photocurrent for these structures, it is apparent that such a reflection correction affects equally the textured interface and its consequent TrO structure. While this is obvious in a certain sense, it further reinforces the idea that one could benefit from mapping the textured interface using concepts from TrO.

Table 4. Comparison of photocurrent for periodic and disordered structures after accounting for escape losses from Air-EVA interface.

J_{ph} (mA/cm^2)	Periodic		Disordered	
	Texture	TrO	Texture	TrO
300-500 nm	5.64	5.73	5.18	5.21
500-1100 nm	14.41	12.52	17.35	14.73
300-1100 nm	20.05	18.25	22.53	19.94

9. Conclusion

We explore the idea of using principles of TrO to come up with an inhomogeneous refractive index structures for light-trapping, which can be directly integrated to a planar absorbing medium. This design tackles the degradation of the electrical properties of the optoelectronic device due to increased surface recombination from surface nanotexturing. The results indicate that with careful choice of texture properties, its equivalent planar structure can enhance absorbance in the planar c-Si wafer close to the textured c-Si counterpart and also outperform a broadband gradient AR coating with a similar refractive index range. Best results are reported for structures with a disorder where both the texture and its planar counterpart approach the Lambertian limit for 1D textured interface. To experimentally realize an index distribution as shown in Fig. 3(b), one can seek the use of electron-beam lithography or self-assembly techniques for patterning characteristic features of high refractive index and atomic-layer deposition (ALD) for conformally depositing dielectric materials with a varying ratio over these high-index nanostructures [56]. Such a realization would require the use of available materials with refractive indices smaller than the maximum refractive index permissible in the inhomogeneous structure for this work. While this will negatively impact its overall light-trapping capability, these structures would still find their use for even thinner active layers where a gradient AR coating is insufficient and capitalizing over diffractive elements becomes all the more necessary. Our approach of designing gradient-index structures inspired by TrO for broadband antireflection and light trapping in thin-film solar cells can unlock an alternative way to realize the light-trapping properties of an optimal texture that may not be accessible by present nanofabrication technology.

Funding. Deutsche Forschungsgemeinschaft (RO 3640/11-1 (413644979), WE 4051/26-1 (413644979)); Excellence Cluster 3D Matter Made to Order ((EXC-2082/1-390761711).

Acknowledgments. The authors acknowledge the discussion with Dr. A. Abass in an early stage of the research.

Disclosures. The authors declare no conflicts of interest.

Data Availability. Data underlying the results presented in this paper are not publicly available at this time but may be obtained from the authors upon reasonable request.

References

1. T. Tiedje, E. Yablonovitch, G. D. Cody, and B. G. Brooks, "Limiting efficiency of silicon solar cells," IEEE Trans. Electron Devices **31**(5), 711–716 (1984).
2. P. Campbell, "Enhancement of light absorption from randomizing and geometric textures," J. Opt. Soc. Am. B **10**(12), 2410–2415 (1993).
3. P. Campbell and M. A. Green, "Light trapping properties of pyramidally textured surfaces," J. Appl. Phys. **62**(1), 243–249 (1987).
4. M. Konagai, "Present status and future prospects of silicon thin-film solar cells," Jpn. J. Appl. Phys. **50**, 030001 (2011).
5. R. B. Wehrspohn, U. Rau, and A. Gombert, *Photon management in solar cells* (John Wiley & Sons, 2015).
6. S. Fahr, T. Kirchartz, C. Rockstuhl, and F. Lederer, "Approaching the lambertian limit in randomly textured thin-film solar cells," Opt. Express **19**(S4), A865–A874 (2011).
7. W.-C. Hsu, J. K. Tong, M. S. Branham, Y. Huang, S. Yerci, S. V. Boriskina, and G. Chen, "Mismatched front and back gratings for optimum light trapping in ultra-thin crystalline silicon solar cells," Opt. Commun. **377**, 52–58 (2016).

8. A. Tamang, A. Hongsingthong, V. Jovanov, P. Sichanugrist, B. A. Khan, R. Dewan, M. Konagai, and D. Knipp, "Enhanced photon management in silicon thin film solar cells with different front and back interface texture," Sci. Rep. **6**(1), 29639 (2016).
9. K. Jäger, M. Fischer, R. A. van Swaaij, and M. Zeman, "Designing optimized nano textures for thin-film silicon solar cells," Opt. Express **21**(S4), A656–A668 (2013).
10. F. Pratesi, M. Burresi, F. Riboli, K. Vynck, and D. S. Wiersma, "Disordered photonic structures for light harvesting in solar cells," Opt. Express **21**(S3), A460–A468 (2013).
11. X. Meng, E. Drouard, G. Gomard, R. Peretti, A. Fave, and C. Seassal, "Combined front and back diffraction gratings for broad band light trapping in thin film solar cell," Opt. Express **20**(S5), A560–A571 (2012).
12. A. Bozzola, M. Liscidini, and L. C. Andreani, "Photonic light-trapping versus lambertian limits in thin film silicon solar cells with 1d and 2d periodic patterns," Opt. Express **20**(S2), A224–A244 (2012).
13. M. Gaudig, J. Hirsch, T. Schneider, A. N. Sprafke, J. Ziegler, N. Bernhard, and R. B. Wehrspohn, "Properties of black silicon obtained at room-temperature by different plasma modes," J. Vac. Sci. Technol., A **33**(5), 05E132 (2015).
14. V. E. Ferry, A. Polman, and H. A. Atwater, "Modeling light trapping in nanostructured solar cells," ACS Nano **5**(12), 10055–10064 (2011).
15. Y.-C. Lee, C.-F. Huang, J.-Y. Chang, and M.-L. Wu, "Enhanced light trapping based on guided mode resonance effect for thin-film silicon solar cells with two filling-factor gratings," Opt. Express **16**(11), 7969–7975 (2008).
16. A. Abass, K. Q. Le, A. Alu, M. Burgelman, and B. Maes, "Dual-interface gratings for broadband absorption enhancement in thin-film solar cells," Phys. Rev. B **85**(11), 115449 (2012).
17. M. Otto, M. Algasinger, H. Branz, B. Gesemann, T. Gimpel, K. Füchsel, T. Käsebier, S. Kontermann, S. Koynov, X. Li, V. Naumann, J. Oh, A. N. Sprafke, J. Ziegler, M. Zilk, and R. B. Wehrspohn, "Black silicon photovoltaics," Adv. Opt. Mater. **3**(2), 147–164 (2015).
18. S. H. Zaidi, D. S. Ruby, and J. M. Gee, "Characterization of random reactive ion etched-textured silicon solar cells," IEEE Trans. Electron Devices **48**(6), 1200–1206 (2001).
19. H. Sakai, T. Yoshida, T. Hama, and Y. Ichikawa, "Effects of surface morphology of transparent electrode on the open-circuit voltage in a-si: H solar cells," Jpn. J. Appl. Phys. **29**(Part 1, No. 4), 630–635 (1990).
20. M. Python, D. Dominé, T. Söderström, F. Meillaud, and C. Ballif, "Microcrystalline silicon solar cells: effect of substrate temperature on cracks and their role in post-oxidation," Prog. Photovoltaics **18**(7), 491–499 (2010).
21. M. Otto, M. Kroll, T. Käsebier, R. Salzer, A. Tünnermann, and R. B. Wehrspohn, "Extremely low surface recombination velocities in black silicon passivated by atomic layer deposition," Appl. Phys. Lett. **100**(19), 191603 (2012).
22. J. B. Pendry, D. Schurig, and D. R. Smith, "Controlling electromagnetic fields," Science **312**(5781), 1780–1782 (2006).
23. U. Leonhardt and T. Philbin, *Geometry and light: the science of invisibility* (Courier Corporation, 2010).
24. J. Valentine, J. Li, T. Zentgraf, G. Bartal, and X. Zhang, "An optical cloak made of dielectrics," Nat. Mater. **8**(7), 568–571 (2009).
25. H. Eskandari and T. Tyc, "Controlling refractive index of transformation-optics devices via optical path rescaling," Sci. Rep. **9**(1), 18412 (2019).
26. M. Kadic, S. Guenneau, S. Enoch, P. A. Huidobro, L. Martin-Moreno, F. J. García-Vidal, J. Renger, and R. Quidant, "Transformation plasmonics," Nanophotonics **1**(1), 51–64 (2012).
27. M. Rahm, D. Roberts, J. Pendry, and D. Smith, "Transformation-optical design of adaptive beam bends and beam expanders," Opt. Express **16**(15), 11555–11567 (2008).
28. D. Roberts, M. Rahm, J. Pendry, and D. Smith, "Transformation-optical design of sharp waveguide bends and corners," Appl. Phys. Lett. **93**(25), 251111 (2008).
29. S. Li, Y. Zhou, J. Dong, X. Zhang, E. Cassan, J. Hou, C. Yang, S. Chen, D. Gao, and H. Chen, "Universal multimode waveguide crossing based on transformation optics," Optica **5**(12), 1549–1556 (2018).
30. X. Ni, N. K. Emani, A. V. Kildishev, A. Boltasseva, and V. M. Shalaev, "Broadband light bending with plasmonic nanoantennas," Science **335**(6067), 427 (2012).
31. Y. Luo, D. Y. Lei, S. A. Maier, and J. B. Pendry, "Transformation-optics description of plasmonic nanostructures containing blunt edges/corners: from symmetric to asymmetric edge rounding," ACS Nano **6**(7), 6492–6506 (2012).
32. S. Tao, Y. Zhou, and H. Chen, "Maxwell's fish-eye lenses under schwartz-christoffel mappings," Phys. Rev. A **99**(1), 013837 (2019).
33. N. Kundtz and D. R. Smith, "Extreme-angle broadband metamaterial lens," Nat. Mater. **9**(2), 129–132 (2010).
34. R. Yang, W. Tang, and Y. Hao, "A broadband zone plate lens from transformation optics," Opt. Express **19**(13), 12348–12355 (2011).
35. L. Liang and S. V. Hum, "Wide-angle scannable reflector design using conformal transformation optics," Opt. Express **21**(2), 2133–2146 (2013).
36. M. McCall, J. B. Pendry, V. Galdi, Y. Lai, S. Horsley, J. Li, J. Zhu, R. C. Mitchell-Thomas, O. Quevedo-Teruel, P. Tassin, V. Ginis, E. Martini, G. Minatti, S. Maci, M. Ebrahimpouri, Y. Hao, P. Kinsler, J. Gratus, J. M. Lukens, A. M. Weiner, U. Leonhardt, I. I. Smolyaninov, V. N. Smolyaninova, R. T. Thompson, M. Wegener, M. Kadic, and S. A. Cummer, "Roadmap on transformation optics," J. Opt. **20**(6), 063001 (2018).
37. P. Kinsler and M. W. McCall, "The futures of transformations and metamaterials," Photonics Nanostructures-Fundamentals Appl. **15**, 10–23 (2015).

38. M. F. Schumann, S. Wiesendanger, J. C. Goldschmidt, B. Bläsi, K. Bittkau, U. W. Paetzold, A. Sprafke, R. B. Wehrspohn, C. Rockstuhl, and M. Wegener, “Cloaked contact grids on solar cells by coordinate transformations: designs and prototypes,” Optica **2**(10), 850–853 (2015).
39. M. F. Schumann, M. Langenhorst, M. Smeets, K. Ding, U. W. Paetzold, and M. Wegener, “All-angle invisibility cloaking of contact fingers on solar cells by refractive free-form surfaces,” Adv. Opt. Mater. **5**(17), 1700164 (2017).
40. M. F. Schumann, A. Abass, G. Gomard, S. Wiesendanger, U. Lemmer, M. Wegener, and C. Rockstuhl, “Single-pass and omniangle light extraction from light-emitting diodes using transformation optics,” Opt. Lett. **40**(23), 5626–5629 (2015).
41. D. Eisenhauer, G. Köppel, K. Jäger, D. Chen, O. Shargaieva, P. Sonntag, D. Amkreutz, B. Rech, and C. Becker, “Smooth anti-reflective three-dimensional textures for liquid phase crystallized silicon thin-film solar cells on glass,” Sci. Rep. **7**(1), 2658 (2017).
42. O. Isabella, H. Sai, M. Kondo, and M. Zeman, “Full-wave optoelectrical modeling of optimized flattened light-scattering substrate for high efficiency thin-film silicon solar cells,” Prog. Photovoltaics **22**(6), 671–689 (2014).
43. A. J. Ward and J. B. Pendry, “Refraction and geometry in maxwell’s equations,” J. Mod. Opt. **43**(4), 773–793 (1996).
44. H. T. Nguyen, F. E. Rougieux, B. Mitchell, and D. Macdonald, “Temperature dependence of the band-band absorption coefficient in crystalline silicon from photoluminescence,” J. Appl. Phys. **115**(4), 043710 (2014).
45. Y. Jiang, S. Pillai, and M. A. Green, “Realistic silver optical constants for plasmonics,” Sci. Rep. **6**(1), 30605 (2016).
46. T. A. Driscoll, “Algorithm 756: A matlab toolbox for schwarz-christoffel mapping,” ACM Transactions on Math. Softw. (TOMS) **22**(2), 168–186 (1996).
47. T. A. Driscoll and L. N. Trefethen, *Schwarz-christoffel mapping*, vol. 8 (Cambridge University, 2002).
48. A. Maradudin and T. Michel, “The transverse correlation length for randomly rough surfaces,” J. Stat. Phys. **58**(3-4), 485–501 (1990).
49. V. Freilikher, E. Kanzieper, and A. Maradudin, “Coherent scattering enhancement in systems bounded by rough surfaces,” Phys. Rep. **288**(1-6), 127–204 (1997).
50. P. Kowalczewski, M. Liscidini, and L. C. Andreani, “Light trapping in thin-film solar cells with randomly rough and hybrid textures,” Opt. Express **21**(S5), A808–A820 (2013).
51. F. J. Harris, “On the use of windows for harmonic analysis with the discrete fourier transform,” Proc. IEEE **66**(1), 51–83 (1978).
52. K. Jäger, D. N. Linssen, O. Isabella, and M. Zeman, “Ambiguities in optical simulations of nanotextured thin-film solar cells using the finite-element method,” Opt. Express **23**(19), A1060–A1071 (2015).
53. Z. Yu, A. Raman, and S. Fan, “Fundamental limit of light trapping in grating structures,” Opt. Express **18**(S3), A366–A380 (2010).
54. E. Yablonovitch, “Statistical ray optics,” J. Opt. Soc. Am. **72**(7), 899–907 (1982).
55. K. Jäger, G. Köppel, M. Hammerschmidt, S. Burger, and C. Becker, “On accurate simulations of thin-film solar cells with a thick glass superstrate,” Opt. Express **26**(2), A99–A107 (2018).
56. A. Mackus, A. Bol, and W. Kessels, “The use of atomic layer deposition in advanced nanopatterning,” Nanoscale **6**(19), 10941–10960 (2014).